

Nitrogen Front Evolution in Purged Polymer Electrolyte Membrane Fuel Cell with Dead-Ended Anode

Jason B. Siegel, Stanislav V. Bohac, Anna G. Stefanopoulou, and Serhat Yesilyurt

Abstract—In this paper we model and experimentally verify the evolution of liquid water and nitrogen fronts along the length of the anode channel in a Proton Exchange Membrane Fuel Cell operating with a dead-ended anode that is fed by dry hydrogen. The accumulation of inert nitrogen and liquid water in the anode causes a voltage drop, which is recoverable by purging the anode. Experiments were designed to clarify the effect of N_2 blanketing, water plugging of the channels, and flooding of the GDL. The observation of each phenomenon is facilitated by simultaneous gas chromatography measurements on samples extracted from the anode channel to measure the nitrogen content, and neutron imaging to measure the liquid water distribution. A model of the accumulation is presented which describes the dynamic evolution of a N_2 blanketing front in the anode channel leading to the development of a hydrogen starved region. Prediction of the voltage drop between purge cycles during non-water plugging channel conditions is shown. The model is capable of describing both the two sloped behavior of the voltage decay, and the time at which the steeper slope begins by capturing the effect of H_2 concentration loss, and the area of the H_2 starved region along the anode channel.

I. INTRODUCTION

The dynamic behavior of Fuel Cell (FC) operation under Dead-Ended Anode (DEA) conditions are modeled and measured in this paper. Although flow-through operation is used on both the anode and cathode of most laboratory/experimental hydrogen Proton Exchange Membrane Fuel Cell (PEMFC) systems, the fuel utilization of anode flow-through operation is too low for commercial and portable systems. To increase the flow through utilization anode recirculation is employed, but the required hydrogen grade plumbing and hardware (ejector/blower) adds weight, volume and expense to the

Acknowledgments: This work was supported by The National Science Foundation through CBET-0932509, and the National Institute for Standards and Technology Center for Neutron Research (NCNR). James Marcicki assisted with the data collection. The authors are also grateful for the help we received collecting and analyzing data from Daniel S. Hussey and David L. Jacobson at the NCNR.

system [1], [2]. Additional complexity is also added to the Balance of Plant (BOP) with the use of external humidification to prevent over-drying of the membrane. However, a DEA can be fed with dry hydrogen, which is regulated to maintain anode pressure. In this configuration, hydrogen is supplied at exactly the rate needed to support the reaction. Fuel cell operation with dry hydrogen in a dead-ended system architecture is possible because water crossing through the membrane is enough to humidify the fuel. The use of a pressure regulator, instead of a mass flow controller, and lack of anode inlet humidification can yield a system with lower cost and weight.

The only problem with this architecture is that nitrogen, from air fed into the cathode, can also cross the membrane, driven by the gradient in partial pressure, creating a blanket of N_2 . Water vapor gradients between the humidified cathode and the dry fed anode also drives excess water into the anode, which can cause significant liquid water accumulation. Unlike water vapor whose maximum partial volume is dictated by temperature, liquid can fill the entire free space and block the flow of reactants, also known as channel plugging. The accumulation of liquid water and nitrogen in the anode channel is first observed near the outlet of the channel. Gravity, and gas velocity driven by consumption of hydrogen, both pull these heavier molecules toward the bottom of the channel. As the mass accumulation continues, a stratified pattern which is stabilized by the effect of gravity develops in the channel with a hydrogen rich area sitting above a hydrogen depleted region. The boundary between these regions is a time-varying front, which proceeds upwards toward the inlet [3]. The mass accumulation physically blocks hydrogen gas from reaching the anode catalyst sites, which is the mechanism for the experimentally observed and recoverable voltage degradation [4], [5], [6]. We propose that the accumulation of N_2 and H_2O leads to: first, larger concentration losses due to decreasing hydrogen concentration near the bottom of the anode channel; then,

shrinking effective area of the cell, and larger activation potential in the cathode. This two-stage mechanism is clearly visible in all experimental conditions, and scales with operating conditions such as load current density, relative humidity, and stoichiometric ratio in the cathode.

Purges of the anode channel volume are necessary to clear the reaction product and inert gas from the channel. An anode purge event consist of opening a downstream solenoid valve, which creates a brief, high velocity flow through the anode removing liquid water and nitrogen. After the purge, the catalyst area contributing to the reaction increases, and hence the measured voltage increases. Understanding, modeling, and predicting the front evolution and overall dynamics in DEA FC would allow judicious choice of purging interval and duration. Better purging strategy can reduce the H_2 wasted during purges and avoid over-drying the membrane. The operation of a PEMFC with hydrogen starved areas can also lead to carbon corrosion [7], [8], [9]; therefore, study of these operating conditions and derivation of controllers to schedule anode purges are critical for DEA operation, and prolonging stack life.

For a fixed purge period and duration, the fuel cell reaches a stable cyclic behavior, typically within a few purge periods, with both consistently repeatable voltage degradation rates between purges and voltage recovery with each purge. We verified the repeatability of the front evolution with in-situ neutron imaging, measuring the liquid water front, and Gas Chromatography (GC), measuring the hydrogen and nitrogen concentration at a specific location in the anode channel, as shown in Fig. 1, which will be discussed later. Gravity, buoyancy, and channel orientation help establish these statistically repeatable and large spatiotemporal variations with hydrogen starvation fronts. Figure 2 shows typical spatial and temporal patterns of liquid water thickness and associated measurements during DEA operation with infrequent anode purging events. The stratification of the hydrogen/nitrogen fronts and the gravity-driven liquid water in the channels also provide a unique modeling paradigm and distinct conditions augmenting earlier work [10], [11], [6], [12], [13], [14] that has not been studied extensively before despite several strictly experimental results [15], [16], [17].

This paper will elucidate dead-ended anode hydrogen PEMFC behavior; specifically, we first introduce the experimental setup, examine the data, and then propose a simple along-the-channel model. We use the model to explain the observed voltage behavior during dead-ended anode operation. Since accumulation of both liquid water and nitrogen in the anode channel of a PEMFC operating under dead ended conditions contribute to the recov-

erable voltage degradation, we devised experiments to characterize the relative effects of both constituents using simultaneous in-situ measurements of both nitrogen and liquid water. Anode purges and cathode surges when coupled with voltage measurement can be used as a diagnostic tool for determining the location of water flooding and the impact of nitrogen blanketing in the anode channel. An anode purge, which is short duration, high flow rate of gas though the anode initiated by opening a downstream valve, removes both liquid water and nitrogen gas from the anode channel and recovers the voltage drop caused by reduced active area on the anode side. A cathode surge is a momentary increase in the air flow rate supplied to the cathode. The excess air increases the partial pressure of oxygen in the channel which leads to increased voltage for the duration of the surge. The excess air flow rate can also remove water from the cathode channel and cathode GDL, which leads to an improvement of the fuel cell voltage after the surge relative to the value before initiating the surge.

Finally, we compare the data with a model that captures the relative impact of each process on the measured cell voltage. In Ref. [3], the effects of nitrogen accumulation driven by convection were investigated, but we improve upon this work by inclusion of diffusive terms in the anode channel and a physics based voltage model which accounts for membrane water content with a distributed current density. By correlating measurements of voltage, liquid water mass, and anode channel gas concentration, we aim to develop and validate a model of PEMFC under DEA operating conditions. Once properly calibrated, this model can be used for anode purge scheduling and stack health monitoring. Snapshots of the data are presented to demonstrate the repeatability of the observed phenomena, and to provide comparisons with the model. In order to prevent confusion and clarify the observed phenomena, the term *flooding* will be used to describe the accumulation of liquid water in the GDL or catalyst layer and the term *plugging* will be used to refer to liquid water in the channels, which blocks or hinders the flow of gas through the channels [18]. The term *blanketing* is used to designate N_2 mass accumulation in the anode channel, which prevents hydrogen from reaching the catalyst layer.

II. EXPERIMENTAL SETUP

A Shimadzu GC-17A Gas Chromatograph was used to measure the hydrogen, nitrogen, and oxygen content of gas samples taken from the anode channel of a PEMFC during dead-ended operation. Simultaneous measurement of the liquid water distribution inside the

fuel cell was acquired via neutron imaging at the National Institute for Standards and Technology (NIST), in Gaithersburg, MD [19], [6].

A. Configuration & Operating Conditions

The tested fuel cell has an active area of 50 cm². The anode gas flow path consist of 25 parallel straight channels with a depth of 1.78 mm and width of 2.08 mm. The anode land width is 0.838 mm, and the channel length is 7.3 cm. The anode channels are oriented on a 45 degree angle and connected at the top and bottom of each channel by a manifold, as shown in Fig. 1. A supply of dry pressure regulated hydrogen, at 4.5 Psi gauge, is fed to the dead-ended anode. As hydrogen is consumed in the reaction, the pressure regulator maintains constant pressure in the anode channel, effectively maintaining operation at hydrogen utilization of one. A solenoid valve located downstream of the fuel cell anode can be periodically opened to purge the anode volume as shown in Fig. 1. This valve is referred to as the Purge Valve (PV). An adjustable valve is located downstream from the anode PV to reduce the pressure drop and flow during a purge. The valve was adjusted prior to starting the experiment and remained fixed. The steady state flow rate, during purging, was measured to be approximately 1 SLPM of Hydrogen. The value, N_{purge} , listed in Table III, is used to model this outlet flow. Note that due to the small diameter passageway between the anode channels and the outlet manifold of the FC, liquid water may impede the flow of gases during the initial portion of a purge. Another solenoid valve is located downstream, connected by capillary tubing, to allow gas sampling from the anode channel. This solenoid valve is referred to as the Sampling Valve (SV) and is described in section II-B. A micro-controller was used to actuate the solenoid valves precisely in time and control the purge event period and duration.

A traditional flow-through architecture with air was used on the cathode side with a bubbler-type humidifier. A backpressure regulator downstream from the cathode maintained the pressure between 3.5 and 4.5 Psig, depending on flow rate. The cathode channels have a 9-pass semi-serpentine flow path consisting of 5 parallel channels. Typical cathode flow rates range from Stoichiometric Ratio (SR) 1.5-3 (oxygen supplied / oxygen consumed). Note that due to the use of air on the cathode, the gas velocities in the channel are much higher than a system running on pure oxygen at the same SR. The Relative Humidity (RH) of the gas stream was varied between 50% and 100%. Cathode surges, which are short duration (1-2 s) increases in the air flow rate (up

to SR 10), were used during the experiment to remove liquid water from the cathode channels and to diagnose the extent of cathode channel plugging. The cathode flow field is aligned perpendicular to the anode channels, but the inlets and outlets are co-located at the upper and lower corners of the cell respectively. As a result the system behavior can be approximated by an equivalent co-flow model as discussed in Sec. IV.

B. Gas Chromatography Setup

The setup shown in Fig. 1 illustrates the interconnection of the GC equipment and fuel cell. A heated capillary tube is inserted into the last anode channel (near the edge of the cell), 3 cm from the bottom corner, as shown in Fig. 1. The 0.005" diameter capillary tube is connected to an electrically actuated six-port rotational valve. A sampling solenoid valve (SV) is placed downstream from the six-port valve, which when opened allows for filling of the sample loop from the fuel cell anode channel when the six-port valve is in position A. After a sample is collected in the sample loop, and SV is closed, the six-port valve is rotated to position B, and the high-pressure carrier gas (helium) pushes the sample into the GC for analysis.

Ultra High Purity (UHP) helium was used as the carrier gas, and supplied at a pressure of 200 kPa gauge. This produced a steady flow of 12 ml per minute to the GC. A Thermal Conductivity Detector (TCD) was used for gas detection. As a result of the choice of column (Heyesep D column Restek 100/120 mesh, 3 m length 1 mm ID), measurement of water vapor was not possible due to the very long elution time for water in the column. The difference in retention times of the GC for hydrogen and nitrogen measurement constrained the maximum sampling rate at one sample every 40 s. The sampling valve is opened for 1 s, during which time approximately 300 μ l of gas is removed from the anode channel (hence the sample volume is less than 5% of the total anode volume). The total anode volume is 6500 μ l. Only the last 5 μ l of the sample are trapped in the sample loop and then pushed into the GC when the six port valve is rotated. The capillary tubing, six-port sampling valve, and sample loop were maintained at a constant temperature of 110 °C, to ensure that a consistent sample concentration was delivered to the GC, and to prevent condensation in the tubing. Details on the GC calibration can be found in the Appendix.

C. Neutron Radiography

Neutron radiography is an in-situ, non-destructive test that involves placing the fuel cell in a beam of neutrons

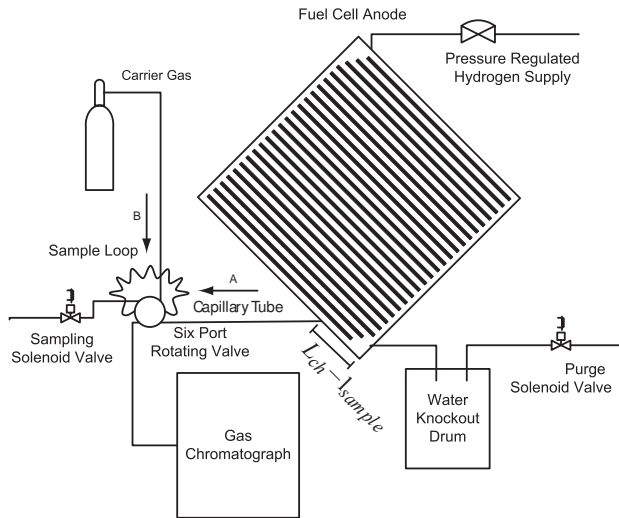


Fig. 1. Illustration of anode flow-field orientation and GC setup with six-port rotating valve. In position A, the flow through the sample loop is from right to left; the Fuel Cell is connected to the Sample Loop (SL) and Sampling Valve (SV), while the carrier gas flows to the GC. In position B, the flow through the sample loop is from top to bottom; the carrier gas is connected to the SL and GC, while the Fuel cell is connected to the SV.

and measuring the change in beam intensity as it passes through the fuel cell. The decrease in beam intensity is caused primarily by neutron interaction with liquid water in the fuel cell. By comparing the image intensity with that of a known dry fuel cell, the two-Dimensional (2-D) distribution of liquid water thickness values in the plane perpendicular to the beam can be calculated [6], [20]. Six of these processed images, showing water thickness values in mm, are presented in Fig. 2, where the images were selected from the data set shown in Fig. 3. Fig. 2(a) and Fig. 2(b) clearly show anode channel water accumulation and the effectiveness of the anode purge in removing water from the channel. Fig. 2(e) and Fig. 2(f) show the effect of cathode surge at removing water from plugged cathode channels. Fig. 2(c) and Fig. 2(d) show the small reduction of the anode channel water plugging, which occurred during repeated anode sampling. During this period voltage continuously improves, as shown in Fig. 3, which is the combined effect of nitrogen and liquid water removal from the channel. Nitrogen is removed with the gas sample, and liquid water droplets are dislodged by the pressure variations in the channel due to the sampling and fall to the bottom of the channel via gravity.

The time-series sequence of neutron images are further processed in two ways, so that the amount of data is reduced and the relevant features are easier to visualize over time. The first method of data reduction is to

estimate the total liquid water mass in each of the three layers, the Cathode Channel (CA CH), Anode Channel (AN CH), and the combined membrane/GDL sandwich layer, by comparing the local water distributions corresponding to the different combinations of channels and lands as described in Ref. [6]. These values are shown in the fifth and sixth subplots of Fig. 3 and Fig. 4, and help identify the presence of GDL water flooding or channel water plugging. To make an inference about the channel water mass, from the 2-D projection of water distribution in the fuel cell, we must assume that locally the GDL water content is uniform in the rib and channel areas. If this assumption is not valid the algorithm used will over-estimate the GDL water content (attributing too much of the measured water mass to the GDL), and under estimate the channel water content, especially in the cathode GDL since CFD models have demonstrated water accumulation to be greater under the ribs [21] for single serpentine co-flow channels under certain operating conditions. Another plausible scenario is that the high gas flow rate in the cathode channel could have a venturi effect, drawing liquid from the GDL, when the water saturation is above the immobile limit, which could explain the correlation in water removal. It is not possible to determine if the correlation (a decrease in total water masses) between the GDL and cathode channel during a surge, shown in Fig. 3 at $t=3400$ s, is physical or an artifact given the current set of measurements. Future work, using neutron imaging with the beam-direction parallel to the membrane will be used to investigate the relationship between GDL and channel liquid water removal. Note that this uncertainty in the location of water accumulation does not impact the nitrogen accumulation or voltage degradation rates measured or modeled in this paper, and we have chosen conditions with less channel water accumulation for model validation.

The second method of analysis quantifies the fractional area coverage by liquid water, and is shown in the seventh subplot of Fig. 3 and Fig. 4. Hence the image processing provides information for (a) the total liquid water mass which is a volume average along the path of the beam at a specific time and (b) information about the distribution of water within the fuel cell, specifically the membrane area which is exposed to liquid water. This additional information is important for modeling because of the difference in membrane properties, proton conductivity and permeation rate, as a function of membrane water content. The fractional area coverage is calculated for two different water thickness values, water thickness values greater than 0.3 mm indicate the presence of water in the channels, and water thickness

greater than 0.05 mm are chosen to indicate the start of GDL hydration which also indicates an area with higher membrane water content.

III. EXPERIMENTAL RESULTS

The data listed in Fig. 3-4 represent the dynamic responses of a PEMFC, there are changes in air-flow, current density, cathode inlet relative humidity and temperature, as indicated in the upper sub-plots of these figures. In the time period prior to what is shown in Fig. 3, the fuel cell was operating for several hours at 55°C, with a low current density (0.2 and 0.4 A cm⁻²), and a fully humidified cathode inlet. The data in Fig. 4 follows Fig. 3 after the cell has been drying at 50% cathode inlet RH for one hour.

The repeatable, and recoverable voltage decay, which is caused by mass accumulation in the anode, can be seen in the voltage plot, with the solid line type in the fifth subplot of Fig. 3 and Fig. 4. The anode purge events indicated by the black vertical lines in the fourth subplot, precede each of the largest voltage improvements. Cathode surges are also correlated with voltage improvement as discussed in the following section.

An important feature of the observed voltage dynamic is the two-sloped decay. A slow initial decay, which can be attributed to dilution of hydrogen in the anode, is followed by a steeper linear decay, which marks the development of a hydrogen depleted region that is covered by a blanketing N₂ front moving upwards toward the inlet. Various operating conditions are selected to demonstrate the complex phenomena occurring during DEA operation.

Table I summarizes the operating conditions depicted in the following figures and discussion. The operating conditions are described using the following notation: (*i#_T#_SR#_RH#*), where the number following *i* denotes the current density in (A cm⁻²), T represents temperature (C), SR is the cathode stoichiometry, and RH is the cathode inlet relative humidity. The data sets, are available online at <http://orion.engin.umich.edu>.

Both N₂ blanketing and liquid water plugging could displace H₂, preventing it from reaching the catalyst sites. In order to study the relative effects of both constituents we identify portions of the data set corresponding to conditions with and without anode water accumulation. In this work, lower cathode inlet RH (60%) cases are used for the investigation of a single phase channel model, hence the influence of N₂ accumulation on voltage can be separately identified. The lack of anode channel plugging is verified from the neutron radiography data.

The operating conditions for Case 5 are (*i*0.4_T60_SR3_RH60) shown in Table I, which are medium current density, 60° C, and high flow rate of sub-saturated air supplied to the cathode. This case is shown in Fig. 4, and is chosen to represent a single phase condition for model comparison in section V.

TABLE I
SELECT CASES FROM DATA SET FOR MODEL COMPARISON

T=30°C	RH \ SR	Low (2)	High (3)
	Full	[1], 8	[6], (7)
Mid			

T=60°C	RH \ SR	Low (2)	High (3)
	Full	11	[2], (9), [10]
Mid			

T=65°C	RH \ SR	Low (2)	High (3)
	Full		
Mid	3, [4]	[5]	

OPC x	Current Density
(x)	0.2 A cm ⁻²
[x]	0.4 A cm ⁻²
x	0.6 A cm ⁻²

A. Cathode Surges versus Anode Purges

In dead-ended anode operation of PEMFCs, anode purges and cathode surges when coupled with voltage measurement can be used as a diagnostic tool for determining the location of water flooding and the impact of nitrogen blanketing in the anode channel. An anode purge, which is short duration, high flow rate of gas though the anode initiated by opening the PV, removes both liquid water and nitrogen gas from the anode channel and recovers the voltage drop caused by reduced active area on the anode side. A representative section of our experiments is shown in in Fig. 3. The first anode purge at t=680 s removes approximately 0.19 g of liquid water from the anode channel and the voltage improves by approximately 130 mV following the anode purge as shown in the fifth subplot of Fig. 3. Neutron images from before, Fig. 2(a), and after, Fig. 2(b), the purge confirm the removal of liquid water from the anode channel.

A cathode surge is a momentary increase in the air flow rate supplied to the cathode. The excess air increases the partial pressure of oxygen in the channel which leads to an increase in the measured cell voltage for the duration of the surge. The excess air flow rate also removes water from the cathode channel and cathode GDL, which leads to an improvement of the fuel cell voltage after the surge relative to the value before initiating the surge. This change in voltage should be related to the amount of water removed from the cathode channel, GDL, or catalyst layer. Also, the resistance to O₂ transport between the channel and the cathode catalyst layer is reported to be large especially for carbon cloth GDLs [22], and cathode purges effectively enhance the O₂ transport to those areas, especially under the rib. Cathode surges, indicated by the short duration spikes in Cathode Stoichiometric Ratio (CA SR) in the second

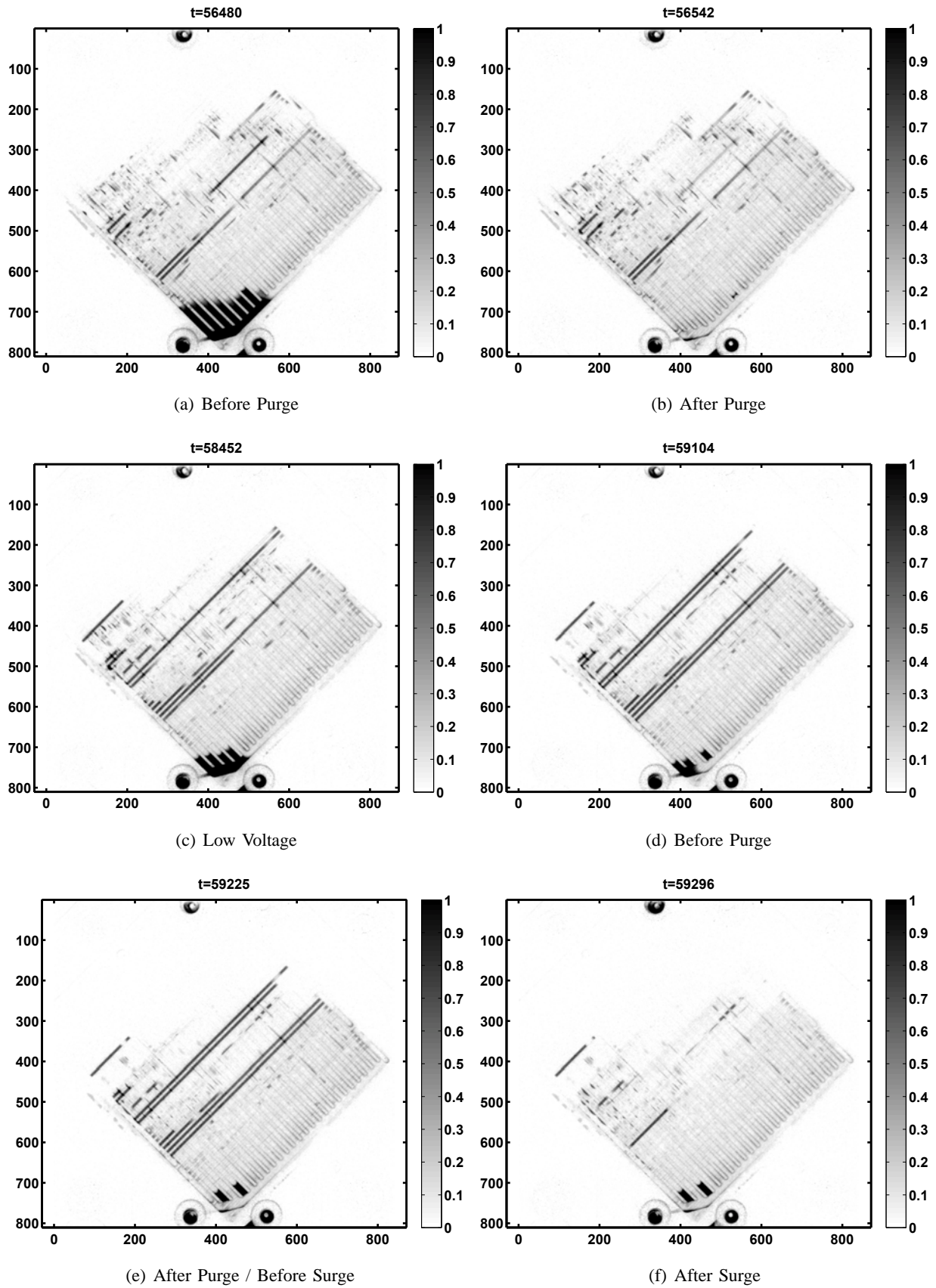


Fig. 2. Neutron images corresponding to the events shown in Fig. 3, from sequential purge cycles. Image intensity represents liquid water thickness in mm.

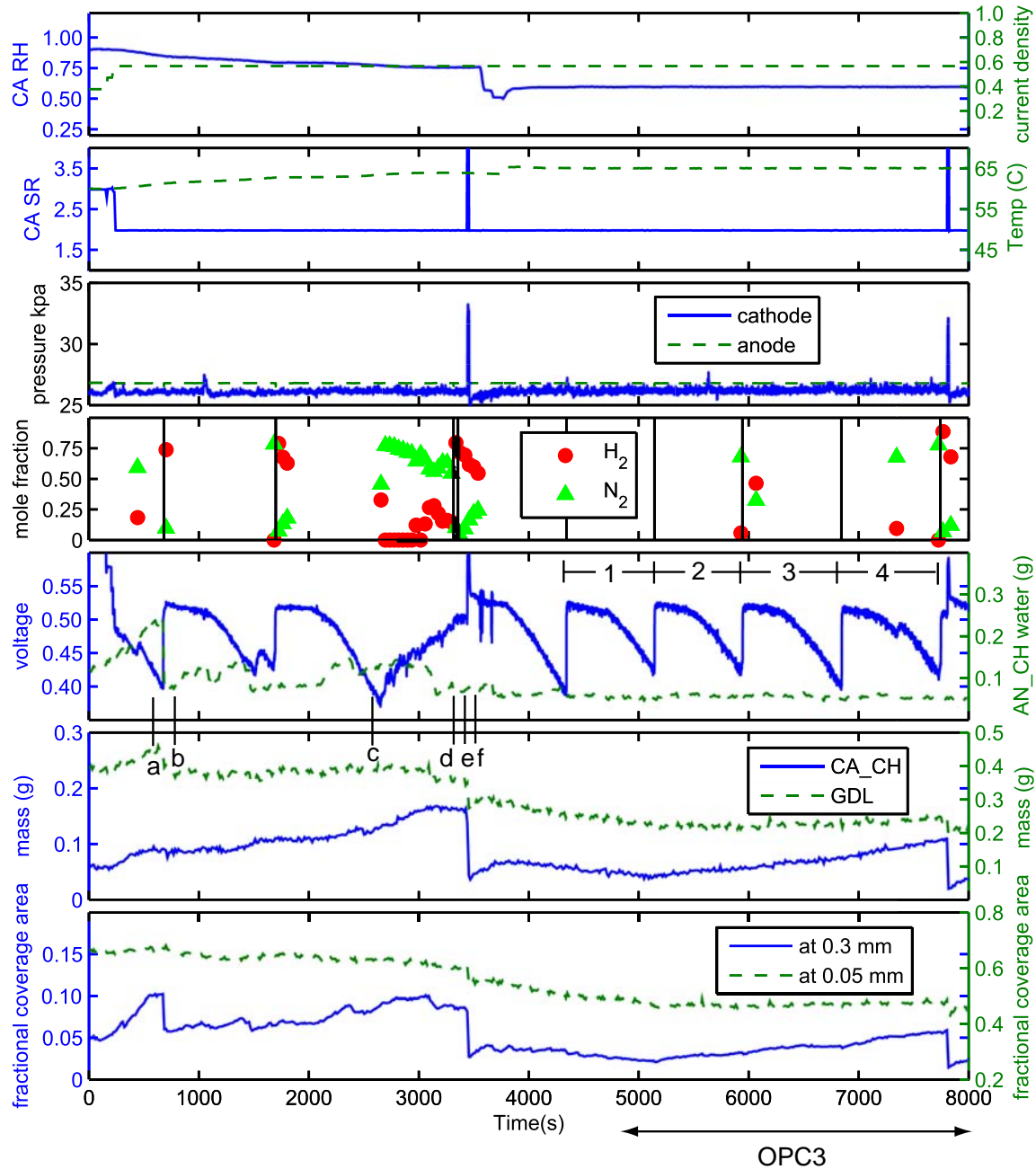


Fig. 3. Operating conditions and processed liquid water data from neutron images, corresponding to initial experiment time $t_0=55800$ s. The dashed (green) lines correspond to the axis on the right, and solid (blue) lines use the left axis. The top subplot shows cathode relative humidity as a fraction (0-1), solid line, and current density ($A\text{ cm}^{-2}$), dashed line. The second subplot shows cathode stoichiometric ratio, solid line, and cell temperature (C), dashed line. The third subplot shows cathode, solid line, and anode channel pressure (kPa gauge), dashed line. The fourth subplot shows the mole fraction of hydrogen and nitrogen that was measured from GC sampling, and the vertical lines indicate anode purge events. The fifth subplot shows the cell voltage, solid line, and the estimated mass of liquid water in the anode channel, dashed line. The letters (a-f) indicate the times at which neutron images (a-f) in Fig. 2 were acquired. The sixth subplot shows the estimated cathode channel liquid water mass, solid line, and GDL mass (g), dashed line. Finally the seventh subplot show the fractional fuel cell area, from neutron imaging, with a measured liquid water thickness greater than 0.3 mm or 0.05 mm.

subplot of Fig. 3, $t = 3400$ s and $t = 7800$ s cause a temporary increase in cathode back-pressure and voltage

and fifth subplots of Fig. 3 respectively. The surge at $t = 3700$ s recovers 36 mV of voltage, and the removal of liquid water from the cathode channel can be clearly

seen by comparing Fig. 2(e) from before the surge to Fig. 2(f) after. Larger voltage recovery from both surges and purges is expected at high current density (0.6 A cm^{-2}), both because of the higher amount of cathode flooding and the greater effect the accumulated water has on voltage output, since a higher local current density leads to lower overall electrochemical efficiency. The fractional coverage area at 0.3 mm , shown as the solid line in the last subplot of Fig. 3, decreases with both anode purges and cathode surges that remove water from the channels, since water thickness values above this threshold are attributed to channel accumulation. The estimates of channel water mass shown in the above subplots are well correlated with the surges, purges and voltage recoveries.

B. Temperature effects

The overall effect of temperature on fuel cell voltage is difficult to quantify, since temperature influences several competing factors. For example increased temperature leads to faster reaction kinetics and increased proton conductivity which both increase voltage. However, the increase in vapor pressure also decreases the oxygen partial pressure which decreases voltage. So, the overall effect may be a decrease in voltage. Temperature also impacts the nitrogen crossover rate through the membrane. The nitrogen permeation rate, k_{N_2} in (30), increases exponentially with temperature. Saturation pressure also increases exponentially with temperature, so the partial pressure of water vapor will be small at lower temperatures.

The slow decrease in cathode inlet RH, shown in Fig. 3, from $t=200 \text{ s}$ to $t=3200 \text{ s}$ following the increase in current density, can be attributed to the increased heat generation which leads to a higher cell temperature than the setpoint value (60° C), while the dewpoint of the inlet air stream remained constant. This sub-saturated cathode air feed leads to a slight recession of the two phase front location as shown in the seventh subplot by the fractional coverage area, even though the decrease in CA SR keeps the gas velocity in the channel close to the previous value after considering the increase in current density. Finally the decrease in cathode RH and increased cell temperature at beginning at $t=3800 \text{ s}$ leads to a more rapid drying of the fuel cell.

The high temperature and low cathode inlet RH conditions shown in the first half of Fig. 4 lead to a dry condition within the fuel cell. The total water mass is very low and the fractional water coverage is also low, indicating that the transition from sub-saturated to saturated conditions along the length of the co-flow

channels is near the outlet. After the transition to lower cell temperature at $t=3700 \text{ s}$, which increases the cathode inlet RH from 60% to 100%, the two phase front moves back toward the inlet as indicated by the increase of the fractional area coverage ($> 0.05 \text{ mm}$). This leads to the onset of both anode channel plugging and cathode channel plugging. When the channels are not plugged the cathode surge at $t=3500 \text{ s}$ has no sustained effect on voltage, but the surges following the increase to fully humidified cathode inlet conditions at $t=5100 \text{ s}$ and $t=7000 \text{ s}$ see voltage improvement that is well correlated with the water removal from the cathode channel. data indicates that GDL water accumulation (data points taken from under the lands) precedes the accumulation of water in the channels.

C. GC sampling effects

The intent of GC sampling was to measure the nitrogen accumulation in the anode channel. The measurement however, modifies the system behavior. Specifically the effect of GC sampling, that is the removal of gas from the anode channel, can improve the FC voltage. When a sample removes accumulated nitrogen or water, from near the end of the anode channel, it is replaced by pure hydrogen flow from the inlet.

GC samples were initiated typically right before and after each purge event and sometimes in the middle of a purge period as shown in the fourth subplot of Fig. 3. Individual GC sampling events are correlated with the small voltage increases shown in the fifth subplot of Fig. 3. A series of samples, between $t = 2700 - 3500 \text{ s}$, were taken at the fastest sampling rate of the GC detector.

Notice that the effect of sampling has more impact on voltage with increasing time since the last anode purge event. This can be explained by nitrogen accumulation model presented in Sec. IV. Samples taken from later in the cycle, allow more nitrogen to accumulate in the anode channel, see for example the sample taken at $t=350 \text{ s}$ in Fig. 3. If the nitrogen does not have sufficient time to accumulate the sample is removing primarily hydrogen from the channel and no voltage improvement is observed, see for example the sample taken at $t=700 \text{ s}$ immediately following an anode purge.

The continuous sampling, at 1 sample every 40 s, observed between $t = 2700 - 3500 \text{ s}$ in Fig. 3, is responsible for the voltage recovery observed over that time interval. If the sampling rate is fast enough to remove more volume than the amount of nitrogen which crosses over through the membrane in that time, then the measured voltage increases with each subsequent sample.

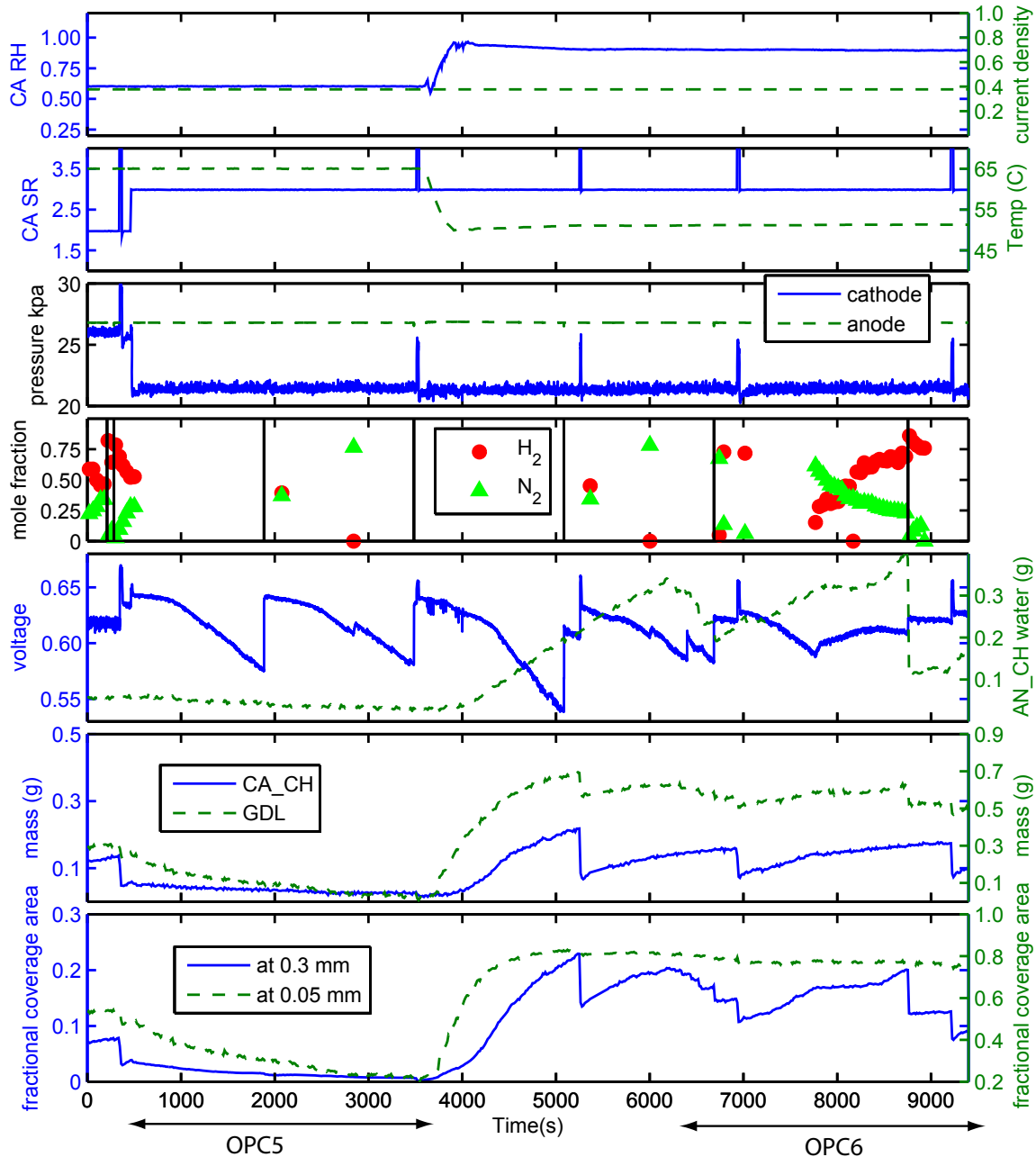


Fig. 4. Selected data set 2 beginning at $t_0=67800$ s, which shows the transition from sub-saturated cathode inlet conditions to fully humidified conditions and the onset of channel plugging.

The fluctuations in anode pressure, due to the repeated sampling, also enhance liquid water removal from the anode channel by allowing liquid water to escape from the channel into the outlet manifold. During normal operation the outlet manifold is at the same pressure at the channel, so there is no flow between these volumes. This explains the drop in anode channel liquid water mass observed between Fig. 2(c) and Fig. 2(d).

D. Voltage Repeatability

The repeatability of several purge cycles, from the end of the larger data set shown in Fig. 3, can be seen by plotting each cycle vs. the time since the previous purge, show in Fig. 5, creating an overlay of the voltage decays with time. The repeatability of the voltage decay characteristics between cycles is remarkable given the fact that some purge cycles contain surge events. Similarly the repeatability and consistency of the measured mole

fractions every purge cycle is very important for modeling and understanding the underlying phenomena. This analysis is useful considering the impact of GC sampling on voltage and nitrogen distribution in the anode channel, the composition of several samples from different points in time during the purge cycle and from different cycles allows us to form an accurate representation of nitrogen accumulation and voltage decay. Notice the nitrogen mole fraction, show in bottom subplot of Fig. 5, saturates at around 0.8, the remaining 20% of the gas is saturated water vapor in the anode channel.

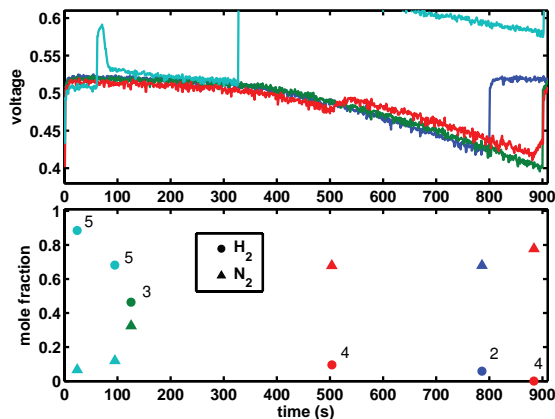


Fig. 5. Subsequent purge cycles are plotted vs. time since the previous purge. The data corresponds to Operating Condition 3, from the larger data set shown in Fig. 3. The numbers 1-5 on the bottom subplot indicate during which purge cycle each GC sample was taken.

IV. MODELING

In this section a one dimensional model of nitrogen crossover and accumulation in the anode channel of a DEA PEMFC is presented. The modeling domain for this work is the anode channel, and membrane. Nitrogen crossing through the membrane, into the anode channel, is pushed to the end of the channel by the convective velocity [3]. The convective velocity is the result of hydrogen consumption, and therefore the velocity will be greatest near the anode inlet, decreasing along the length of the channel. Due to the high diffusivity of hydrogen in the anode channel, we use the Stefan Maxwell equation to describe the nitrogen distribution along the channel, resulting from both convection and diffusion, for comparison with the measured mole fractions from GC sampling. A physics based voltage model is used to account for the distributed current density, and hydrogen consumption rate. The voltage model includes the effect of membrane water content and proton concentration. We consider an isothermal modeling approach, and the measured cell end-plate temperature is used for T .

The important dimensions for channel modeling are x , the through membrane direction, and y , the along the channel direction as shown in Fig. 6. For the anode, the spatial variation of gas concentrations in the x -direction is considered, but the steady-state gas diffusion profiles are calculated and used to propagate the channel values (which are modeled as dynamic states) across the GDL to the surface of the membrane. A similar decoupling between the x and y distributions is proposed in [23], to address the computational complexity and to take advantage of the very different length scales. On the cathode, only the steady state profiles are considered for modeling both the x and y -dimensions. The approximation of steady state distributions is appropriate for the cathode gas channel due to the high gas flow rate and the large time scales over which the anode dynamics evolve.

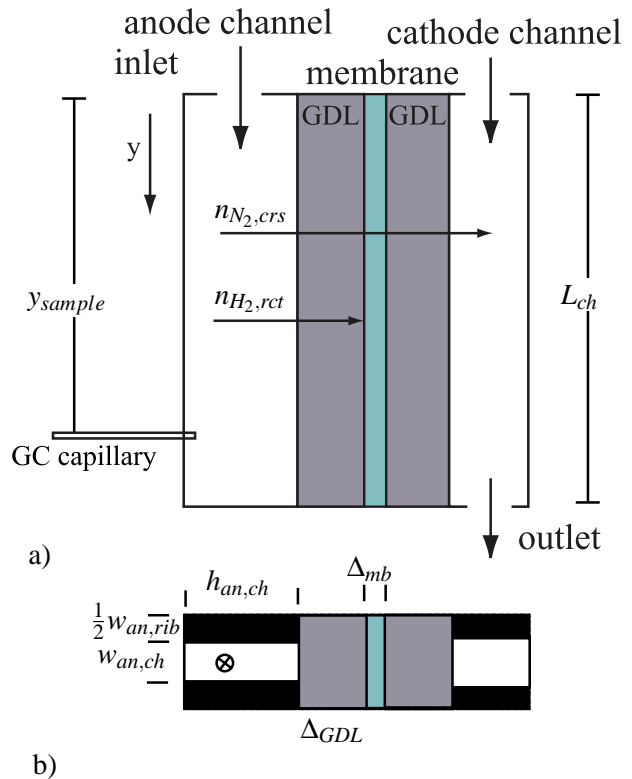


Fig. 6. a) One dimensional fuel cell modeling domain, y denotes the distance along the channel from inlet to outlet (not drawn to scale). b) fuel cell channel dimensions.

The constants, listed in Table III, and equations describing the gas constituents in the channels are written using SI units. The exceptions are the related parameters in the voltage model, Table II, which use A cm^{-2} consistent with the fuel cell literature. In the along the channel model, the fluxes n have units ($\text{mol m}^{-1} \text{s}^{-1}$), and flows N (mol s^{-1}).

A. Nitrogen Accumulation (single phase along the channel model).

In order to consider both water, and nitrogen transport through the membrane, our modeling effort requires considering a ternary system for the anode. The Stefan Maxwell Model (SMM) describes convection, diffusion and reactions in the gas-channel,

$$\frac{P_{an}}{RT} \frac{\partial x_i}{\partial t} = -\frac{\partial}{\partial y} (J_i + x_i N_t) + r_i, \quad (1)$$

for $i = [1, 2]$, where N_t is the total gas flux, J_i is the diffusive flux, and r_i denotes the reaction terms. Only two of the three components are independent in this modeling framework. We chose the mole fractions of nitrogen, $x_{N_2} = x_1$, and water vapor, $x_{H_2O} = x_2$, as our dynamics states. Since the mole fractions must sum to one,

$$\sum x_i = 1, \quad (2)$$

we can calculate the hydrogen from the other gases $x_{H_2}(y) = 1 - x_{N_2}(y) - x_{H_2O}(y)$. Note that $x_{H_2} = \min(x_2, P_{sat}(T)/P_{an,in})$ is used for all following calculations, including J_i . The remaining water is assumed to be liquid water and is tracked separately, we are assuming instant condensation.

The convective flux, N_t , is driven by the consumption of hydrogen (7). Note that in (1) a constant pressure is used as an approximation, since the anode volume is fed via pressure regulation and the straight channel geometry introduces minimal pressure drop along the length of the channel. Although a pressure gradient, corresponding to the convective flux, develops along the length of the channel, the pressure drop is less than 1 Pa at 1 A cm^{-2} , so a constant pressure is a valid for calculating the concentrations. The ideal gas law, $PV = nRT$ or $P = cRT$, is used to relate pressure and mole fraction of gas species in the channel.

A causal formulation for the diffusive fluxes is used [24],

$$\begin{bmatrix} J_1 \\ J_2 \end{bmatrix} = -\frac{P_{an}}{RT\phi(x)} \begin{bmatrix} D_1(x_1), & D_2(x_1) \\ D_3(x_2), & D_4(x_2) \end{bmatrix} \begin{bmatrix} \frac{\partial x_1}{\partial y} \\ \frac{\partial x_2}{\partial y} \end{bmatrix}, \quad (3)$$

where

$$\begin{aligned} D_1(x_1) &= (1-x_1)D_{13}D_{12} + x_1D_{23}D_{13}, \\ D_2(x_1) &= -x_1(D_{23}D_{12} - D_{23}D_{13}), \\ D_3(x_2) &= -x_2(D_{13}D_{12} - D_{23}D_{13}), \\ D_4(x_2) &= (1-x_2)D_{23}D_{12} + x_2D_{23}D_{13}, \end{aligned} \quad (4)$$

and D_{ij} are the temperature dependent binary diffusion coefficients from [25]. $\phi(x)$ is given by

$$\phi(x) = (D_{23} - D_{12})x_1 + (D_{13} - D_{12})x_2. \quad (5)$$

Conservation of mass allows solving of (1) for $N_t(y)$, assuming the outlet flow is known $N_t(L) = N_{out}$. The equation for conservation of mass can be written as,

$$\frac{\partial N_t}{\partial y} = \sum r_i, \quad (6)$$

since $\sum J_i = 0$ by definition. Then the convective flux along the channel can be found from (6) by integrating backward in space along the channel,

$$N_t(y) = N_t(L) + \int_y^L (n_{H_2,ret}(\tilde{y}) + n_{N_2,crs}(\tilde{y}) + n_{H_2O,crs}(\tilde{y})) d\tilde{y}. \quad (7)$$

Since the anode is dead-ended, $N_{out} = 0$ unless the downstream solenoid valve is open and the anode is purging, in which case $N_{out} = N_{purge}$, a constant.

The source term for nitrogen in the anode channel is membrane crossover, which is calculated from the difference in nitrogen partial pressure across the membrane of thickness Δ_{mb} ,

$$n_{N_2,crs}(y) = -K_{N_2}(T, \lambda_{mb})(w_{an,ch} + w_{an,rib}) \frac{(P_{N_2,ca,mb}(y) - P_{N_2,an,mb}(y))}{\Delta_{mb}}. \quad (8)$$

We assume the permeation takes place both over the ribs, and channels ($w_{an,ch} + w_{an,rib}$), where w_* indicates the width of each. The partial pressure of nitrogen at each membrane surface is calculated using the following expressions, $P_{N_2,an,mb}(y) = x_{N_2}(y) P_{an,in}$ and $P_{N_2,ca,mb}(y) = P_{ca,in} - P_v(T) - P_{O_2,ca,mb}(y)$, assuming uniform pressure and saturated water vapor everywhere. This reasonable considering the water generation rate, especially when humidified inlets are used at low to mid temperatures. The oxygen concentration at the cathode surface of the membrane, $P_{O_2,ca,mb}(y)$, is calculated using (26). The nitrogen permeation rate, $K_{N_2}(T, \lambda_{mb})$, is given by (30), and depends both on temperature and membrane water content.

The hydrogen reaction rate is calculated from the local current density,

$$n_{H_2,ret}(y) = \frac{i_{fc}(y)}{2F}(w_{an,ch} + w_{an,rib}), \quad (9)$$

where F is Faraday's constant.

The source term for water vapor in the anode channel is also membrane crossover, which is calculated from the diffusion and electro-osmotic drag

$$n_{H_2O,crs} = -\left(\frac{\lambda_{ca} - \lambda_{an}}{R_{w,mb}} - n_d(\lambda_{mb}) \frac{i_{fc}}{F}\right)(w_{an,ch} + w_{an,rib}) \quad (10)$$

where $R_{w,mb}$ is the resistance to membrane transport,

$$R_{w,mb} = \frac{\Delta_{mb}}{D_w(\lambda_{mb}, T)} + \frac{1}{k_{ads}} + \frac{1}{k_{des}}, \quad (11)$$

arising from diffusion, where $D_w(\lambda_{mb}, T)$, is water diffusion coefficient for water in the membrane [26], and interfacial mass transfer attributed to membrane adsorption k_{ads} and desorption k_{des} [26], [27], [28]. The coefficient of electro-osmotic drag, $n_d(\lambda_{mb})$, can also be found in [26]. Both D_w and n_d are λ_{mb} dependent and increase with membrane water content.

The membrane water content is the final dynamic state in the model, and is calculated from the difference between the anode and cathode equilibrium lambda values,

$$\frac{\partial \lambda_{mb}(y)}{\partial t} = K_{mb}(\lambda_{an}(y) + \lambda_{ca}(y) - 2\lambda_{mb}(y)) \quad (12)$$

where $K_{mb} = k_{ads}/\Delta_{mb} = 0.25$ is the membrane water uptake rate. Other, more recent models for membrane water uptake [27], [28], will be investigated in future work, but should not impact the results for nitrogen accumulation presented here.

The equilibrium membrane water content is calculated from the water activity using the uptake isotherm [26],

$$\lambda_{an}(y) = c_0(T) + c_1(T)a_{H_2O,an} + c_2(T)a_{H_2O,an}^2 + c_3(T)a_{H_2O,an}^3 \quad (13)$$

where $a_{H_2O,an}(y) = x_{H_2O}(y) P_{an,in}/P_{sat}(T)$.

There exists a coupling between membrane water content, $\lambda_{mb}(y)$, the current density distribution, $i_{fc}(y)$, and nitrogen crossover rate, $K_{N_2}(T, \lambda_{mb})$. The nitrogen permeation rate depends on membrane water content, and the nitrogen accumulation rate depends on both the permeation rate and current density distribution (convective versus diffusive flow). The current density distribution depends on nitrogen accumulation (through blanketing of H_2) and the membrane water content for proton transport losses in membrane. Finally membrane water content depends on the local current density and channel / GDL conditions.

B. Modeling the GC sample location

The flow of gas removed from the anode channel during sampling is modeled by modifying (7), to include the sample flow,

$$N_t(y) = N_t(L) + \int_y^L (n_{H_2,ret}(\tilde{y}) + n_{N_2,crs}(\tilde{y}) + n_{H_2O,crs}(\tilde{y})) d\tilde{y} + \begin{cases} N_{sample} & \text{for } (y \leq y_{sample}) \\ 0 & \text{for } (y > y_{sample}) \end{cases} \quad (14)$$

where y_{sample} is the location of the sampling port along the equivalent channel.

Since the fuel cell is on a 45° angle and each of the anode channels are connected at the top and bottom shown

in Fig. 1, the N_2 blanketing front propagation needs to be transformed for comparison with an equivalent straight single channel. The nitrogen coverage area, on the other hand, can be directly related to the coverage area in the single channel equivalent model. Hence we use the following relationship for the virtual single channel fuel cell sampling location y_{sample} ,

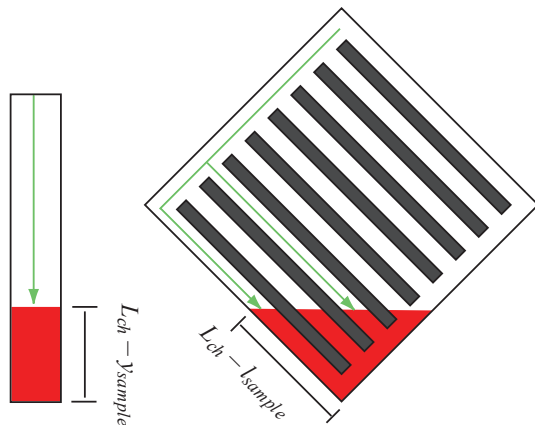


Fig. 7. Mapping anode channels to equivalent single channel. Notice that the path length, in the 45° orientation, to nitrogen front location is the same for all channels.

$$\frac{(L_{ch} - y_{sample})}{L_{ch}} = \frac{(L_{ch} - l_{sample})^2}{2A_{fc}} \quad (15)$$

This equation relates the fractional area below the sampling location for the fuel cell placed in the diagonal orientation (RHS), shown in Fig. 7 to the fractional area below the sampling location in the equivalent model (LHS), shown in Fig. 6. The physical nitrogen sampling location is 3 cm from the bottom edge of the fuel cell along the last channel, $L_{ch} - l_{sample} = 0.03$, as shown in Fig. 7.

C. Distributed Current Density

In previous work, the voltage was calculated based on a uniform apparent current density [29], which is related to the catalyst area with sufficient reactants to support the reaction, i.e. the channel length not covered by nitrogen [3] or water [29]. In this work we consider the distributed current density, which is calculated directly from the reactant concentrations. Although the apparent area modeling technique captured the correct voltage output behavior of the system, the full distributed current density approach is chosen for this work in order to match internal model states, and the measurement of nitrogen molar fraction during sampling from the anode channel at the fixed sampling location, l_{sample} . The diffusion of hydrogen and nitrogen in the anode

channel affects both the current density distribution and GC measurement.

The inputs to the voltage model are: total current $I_{fc}(A)$, temperature T (K), membrane water content distribution $\lambda_{mb}(y)$, hydrogen partial pressure at the membrane surface $P_{H_2,an,mb}(y) = RTc_{H_2,an,mb}(y)$ (Pa), and oxygen partial pressure at the cathode membrane surface $P_{O_2,ca,mb}(y)$ (Pa) which is calculated in (26). The cell terminal voltage is calculated from the open circuit potential minus the concentration, over-potential and ohmic losses.

$$E_{cell} = E_{rev}(y) - \eta_{mb}(y) - \eta_{GDL}(y) - \eta_{act,ca}(y) - \eta_{act,an}(y). \quad (16)$$

Calculation of the fuel cell terminal voltage, and current density distribution requires the additional computation effort to solve N+1 simultaneous non-linear algebraic constraint equations, where N is the number of discretized sections used to solve the PDE system. The distributed current density is resolved by solving the set of N equations (16), for a uniform potential E_{cell} and one equation for conservation of current,

$$\frac{I_{fc}}{A_{fc}} = \frac{1}{L_{ch}} \int_0^{L_{ch}} i_{fc}(y) dy. \quad (17)$$

The reversible voltage is given by,

$$E_{rev}(y) = E_0 - \frac{RT}{nF} \log \left(\frac{a_{H_2O}(y)}{a_{H_2}(y) \sqrt{a_{O_2}(y)}} \right). \quad (18)$$

where $E_0 = 1.229 - (T - T_0) \cdot 2.304 \times 10^{-4}$ [30]. The reactant and product activities are calculated from the concentrations $a_{H_2}(y) = c_{H_2,an,mb}(y)/C_{ref,H_2}$, $a_{O_2}(y) = c_{O_2,ca,mb}(y)/C_{ref,O_2}$ and $a_{H_2O} = 1$ since liquid water product assumed. The subscript *ref* refers to the reference quantity, and subscript *ca,mb* refers to the cathode membrane surface.

In order to simplify the calculation of cell voltage, a hyperbolic sine function is used for the calculation of over-potentials, $\eta_{act,ca}$ and $\eta_{act,an}$, from the exchange current density, $i_{o,ca}(y)$ and $i_{o,an}(y)$,

$$\eta_{act,ca}(y) = \frac{RT}{\alpha_{c,a} nF} \operatorname{asinh} \left(\frac{k_{units} i_{fc}(y) + i_{loss}}{2i_{o,ca}(y)} \right), \quad (19)$$

Where, $k_{units} = 100^{-2} \frac{m^2}{cm^2}$ is for units conversion, $i_{fc}(y)$ is the distributed current density from (17) and i_{loss} is the lost current density due to hydrogen crossover, a tuned parameter which is listed in Table II. The hyperbolic sine is equivalent to the Butler-Volmer equation when the forward and reverse reaction coefficients ($\alpha_{c,a} = \alpha_{c,c}$) are equal [31].

Although the cathode reaction depends on the oxygen concentration as well as the activity of protons in the

membrane [32], the proton activity term is typically neglected since there are sufficiently many protons under fuel cell normal operation. Since we expect low hydrogen concentration in the anode near the end of the channel, we include the proton effect on the exchange current density,

$$i_{o,ca}(y) = i_{o,ref,ca} \left(\frac{c_{O_2,ca,mb}(y)}{C_{ref,O_2}} \right)^{\gamma_{O_2}} \left(\frac{c_{H^+,ca,mb}(y)}{C_{ref,H^+}} \right)^{\gamma_{H^+}} \cdot \exp \left(\frac{-E_c}{R} \left(\frac{1}{T} - \frac{1}{T_0} \right) \right), \quad (20)$$

where $i_{o,ref,ca}$ is the reference current density, c_* is the reactant concentration, γ is the concentration parameter, and E_c in the Arrhenius term is the activation energy for hydrogen oxidation on platinum [33]. The cathode concentration parameter for the local proton activity, $\gamma_{H^+} = 0.5$ is given by [34]. The inclusion of proton concentration is required to capture the effect of nitrogen blanketing in the anode channel, which prevents hydrogen from reaching the catalyst layer to supply protons for the reaction. The cathode exchange current density is proportional to the square-root of the local proton activity at the cathode catalyst layer and the proton activity in the cathode catalyst layer depends on the concentration of protons dissolved in the aqueous phase in the membrane, which is proportional to the square-root of the hydrogen pressure at the anode membrane surface, for low P_{H_2} , [35], therefore we approximate this relationship with a hyperbolic tangent function

$$\left(\frac{c_{H^+,ca,mb}}{C_{ref,H^+}} \right)^{\gamma_{H^+}} = K_{H_2} \tanh \left(100 \frac{c_{H_2,an,mb}}{C_{ref,H_2}} \right). \quad (21)$$

The constant K_{H_2} is absorbed into the reference current density $i_{o,ref,ca}$. At the limit, when the hydrogen concentration is zero, the proton activity at the anode drops to zero. Thus, when the anode is subjected to local fuel starvation, the hydrogen partial pressure drops, hence the proton concentration in the cathode decreases. Furthermore, the membrane electrolyte conductivity also decreases due to lower contribution from the proton conduction in the bulk phase akin to increasing electrolyte resistance due to decreasing ionic concentration [32]. The overall reduction of proton activity at the cathode ultimately leads to a drop in the local current density near the dead-ended exit of the anode. For constant load current (galvanostatic) conditions, as the power production near the outlet shuts down, the current density increases near the anode inlet, where the membrane is relatively dry, which may lead to higher losses and increased temperature.

Similarly for the anode side,

$$\eta_{act,an}(y) = \frac{RT}{\alpha_{a,an} n F} \operatorname{asinh} \left(\frac{k_{units} i_{fc}(y) + i_{loss}}{2i_{o,an}(y)} \right), \quad (22)$$

where the anode exchange current density is,

$$i_{o,an} = i_{o,ref,an} \left(\frac{c_{H_2,an,mb}}{C_{ref,H_2}} \right)^{\gamma_{H_2}} \exp \left(\frac{-E_c}{R} \left(\frac{1}{T} - \frac{1}{T_0} \right) \right). \quad (23)$$

The membrane resistance is calculated as follows,

$$\eta_{mb}(y) = \frac{k_{units} i_{fc}(y) \Delta_{mb}}{\sigma_{mb}(\lambda_{mb}, T) \tanh(100c_{H_2,an,mb}/C_{ref,H_2})} \quad (24)$$

again the hyperbolic tangent is used to approximate the relationship between conductivity and proton concentration [35], and to reflect the effect of increasing electrolyte resistance due to decreasing ion concentration [32]. The membrane conductivity $\sigma_{mb}(\lambda_{mb}, T)$ is a function of water content using the standard relationship from Springer et. al. [36].

Finally the GDL and contact resistances are lumped into R_{GDL} , for the ohmic loss term,

$$\eta_{GDL}(y) = k_{units} i_{fc}(y) R_{GDL} \quad (25)$$

The voltage model was tuned using flow through data from the fuel cell then compared with the experimental voltage degradation rates under dead-ended operating conditions. For model tuning with flow through data, it is assumed that the membrane is fully humidified $\lambda(y) = \lambda(T, a = 1)$, where $\lambda(T, a = 1)$ can be found in [37], and the effects of GDL and cathode catalyst layer flooding are ignored due to the low current density operation.

1) *Along the channel distributions:* Since the oxygen partial pressure in the cathode channel is not currently considered as one of the dynamic states in the model, it is calculated simultaneously with the current density distribution $i_{fc}(y)$ (A/cm²) from the cathode inlet pressure and stoichiometric ratio using

$$P_{O_2,ca,mb}(y) = P_{O_2,ca,in} - \frac{RT}{4F} \left(\frac{i_{fc}(y)}{h_m} + \frac{i_{fc}(y) \Delta_{GDL}}{D_{O_2,eff}} + \int_0^y \frac{i_{fc}(\tilde{y})}{u_{ca,in} h_{ca,ch}} d\tilde{y} \right) \frac{(w_{ca,ch} + w_{ca,rib})}{(w_{ca,ch})} \quad (26)$$

$h_{ca,ch}$ is the cathode channel height, $w_{ca,ch}$ is the cathode channel width and $w_{ca,rib}$ is the cathode rib width. h_m is the interfacial mass transfer coefficient, [31] and $u_{ca,in}$ is the cathode inlet gas velocity (assumed constant along the length of the cathode channel for simplicity),

$$u_{ca,in} = \frac{SR_{ca} I_{fc} (w_{ca,ch} + w_{ca,rib}) L_{ca,ch} (RT)}{(4F) A_{fc} P_{O_2,ca,in} (h_{ca,ch} w_{ca,ch})} \quad (27)$$

where the partial pressure of oxygen at the cathode inlet is given by $P_{O_2,ca,in} = OMF_{ca,in} (P_{ca,in} - P_{v,ca,in})$. $P_{ca,in}$ is the cathode inlet pressure, $P_{v,ca,in}$ is the cathode inlet vapor pressure, $OMF_{ca,in} = 0.21$ is the oxygen molar fraction. SR_{ca} is the cathode stoichiometry.

The cathode vapor pressure along the length of the channel is calculated similarly,

$$P_{H_2O,ca}(y) \approx \min \left(P_{sat}(T), P_{H_2O,ca,in} + \frac{RT}{4F} \int_0^y \frac{i_{fc}(\tilde{y})}{u_{ca,in} h_{ca,ch}} d\tilde{y} \frac{(w_{ca,ch} + w_{ca,rib})}{(w_{ca,ch})} \right). \quad (28)$$

This equation actually needs $+\int n_{H_2O,crs}(\tilde{y}) d\tilde{y}$ to be correct, but then it becomes difficult to solve for the steady state cathode vapor distribution analytically. At high cathode SR this should not be a problem, but may affect the O₂ distribution in low SR, however, this still should be a second order effect compared to variations in the anode.

The anode channel hydrogen concentration is propagated to the membrane surface assuming a simple diffusion model,

$$c_{H_2,an,mb}(y) = \frac{x_{H_2}(y) P_{an,ch}}{(RT)} - \frac{i_{fc}(y) \Delta_{GDL}}{2F D_{H_2,eff}} \frac{(w_{an,ch} + w_{an,rib})}{w_{an,ch}} \quad (29)$$

based on the effective diffusivity $D_{H_2,eff} = D_{eff} D_{H_2,N_2}$ [38].

D. Nitrogen Crossover Rate

Kocha et al. [4] report a large range of nitrogen permeability, over 1 order of magnitude. It has been shown that the permeation increases with both membrane water content and temperature. Temperature has a larger effect on permeability, when the membrane is well hydrated. In this case the permeability can change by a factor of 2-5, over the normal range of operating temperatures 30-60 °C. The nitrogen permeation model, includes the effects of membrane water content and temperature, [39],

$$K_{N_2}(T, \lambda_{mb}) = \alpha_{N_2} (0.0295 + 1.21 f_v - 1.93 f_v^2) \times 10^{-14} \times \exp \left[\frac{E_{N_2}}{R} \left(\frac{1}{T_{ref}} - \frac{1}{T} \right) \right], \quad (30)$$

where $E_{N_2} = 24000$ J mol⁻¹, $T_{ref} = 303$, R is the universal gas constant, and f_v is the volume fraction of water in the membrane, given by;

$$f_v = \frac{\lambda_{mb} V_w}{V_{mb} + \lambda_{mb} V_w} \quad (31)$$

where $V_{mb} = EW/\rho_{mb,dry}$ is the dry membrane volume, equivalent weight divided by density, and V_w is the molar volume of water. λ_{mb} is the membrane water content.

A change in permeability could account for the different nitrogen accumulation rates observed via different voltage drop rates, assuming the voltage degradation is caused by nitrogen accumulation. It should also be noted that the current density would tend to shift toward the inlet, where the membrane is dry and has lower proton conductivity, hence there would be increased resistive losses when N_2 accumulates in the end of the channel.

V. MODELING RESULTS

The PDE, (1), is discretized, using a central difference in space, into $N=50$ sections and solved using an ode solver. The anode channel model is solved using matlab “ode15s”, which supports Differential Algebraic Equations (DAEs), of the form

$$M\dot{z} = f(z). \quad (32)$$

where $z = [x_{N_2,an}, x_{H_2O,an}, \lambda_{mb}, i_{fc}, E_{cell}]^T$, and $M = \text{diag}(I^N, I^N, I^N, 0^N, 0)$, and I^N is the $N \times N$ identity matrix.

Three simulation plots are shown in Figs. 8, 10 and 11 corresponding to operating conditions 3, 5 and 6. These portions of data are contained within the large data sets shown in Figs. 3-4. The first two data sets are chosen to match the model assumptions of humidified channel conditions, but no channel liquid water plugging. The third condition shows some flooding and hence error in the model prediction of voltage, but the overall dynamic voltage behavior is captured quite well by the model ignoring the offset. The first plot in Fig. 8 corresponding to condition 3 shows the measured and predicted voltage in the top subplot and the GC measurement and simulated mole fraction at the sampling location in the bottom subplot. The model demonstrates very good agreement with the data at this operating condition since no anode channel liquid water accumulation was observed during this period. Figure 9 shows the time evolution of the hydrogen mole fraction distribution and membrane water content over a purge cycle. Three snapshots of the distributions, corresponding to $t=1700$ s, $t=2000$ s and $t=2400$ s, from the third cycle in Fig. 8 are shown. The “corner” in the voltage trace at $t=2000$ s, where the rate of voltage degradation increases, indicates that a sufficient amount nitrogen has accumulated in the channel to create a stratified front and a hydrogen starved region develops at the outlet. Finally at $t=2400$ s the nitrogen front has evolved to cover nearly 20% of the anode channel. At this time, the effect of the nitrogen

blanketing is clear, as the current density (the dash-dot line in the third subplot) is shifted.

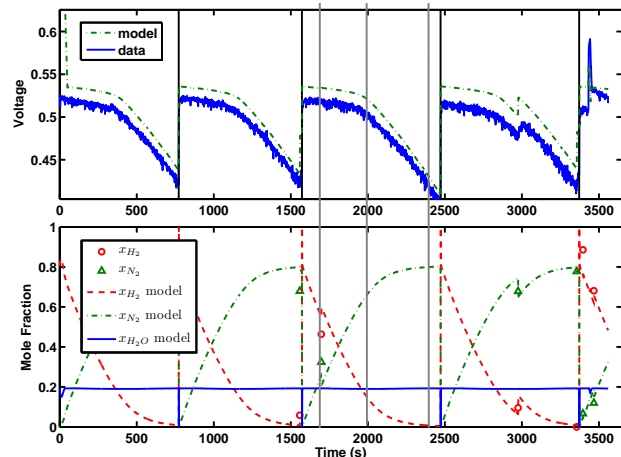


Fig. 8. Operating Condition 3 ($i0.6_T65_SR2_RH60$): Shows very good results with model matching because the assumption of non-water plugging conditions in the channels is satisfied.

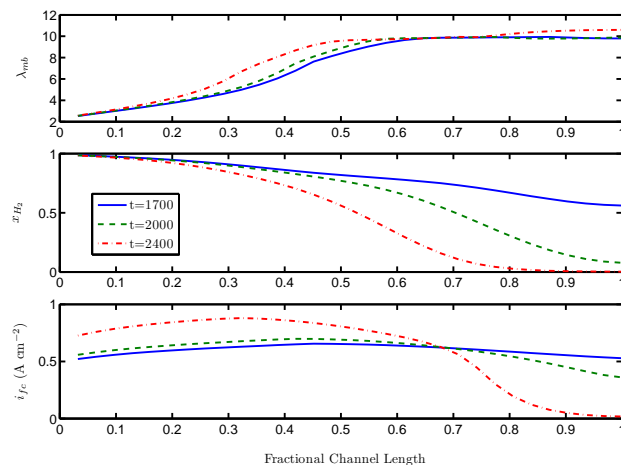


Fig. 9. The first subplot shows a snapshot of the membrane water content along the length of the channel for three times shown in Fig. 8; after a purge, mid cycle and before the next purge. The second subplot shows the hydrogen mole fraction along the length of the channel. The final subplot shows the current density distributions. Notice the front is fully developed at $t=2400$ s, leading to hydrogen starved region covering nearly 20% of the channel.

Operating condition 5 shown in Fig. 10 corresponds higher cathode stoichiometry, and lower current density, therefore we see slightly drier conditions along the channel, but very similar membrane water content behavior to the previous case. The “corner” in the voltage model occurs too late, which indicates that either the diffusion coefficient is too large, or the nitrogen accumulation rate is too low and the membrane resistance is too high since the voltage degradation rate after the corner point is too steep. Notice the effect of GC sampling on

voltage for samples which occur early in the purge cycle compared to later (larger voltage recovery), which the model accurately predicts.

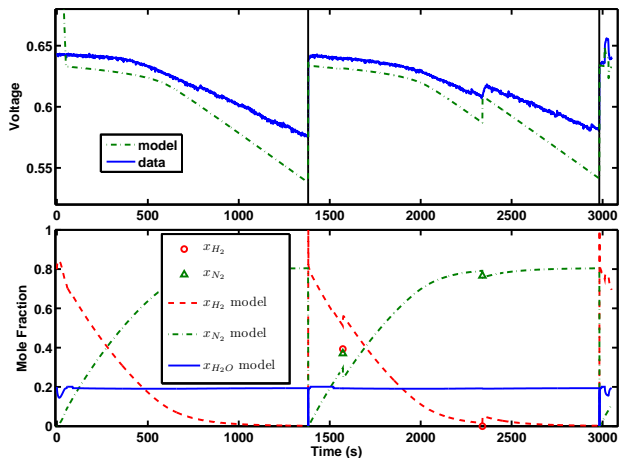


Fig. 10. Operating condition 5 ($i0.4_T60_SR3_RH60$)

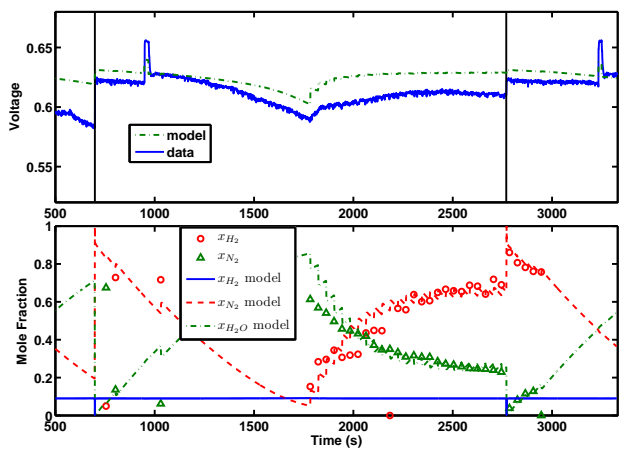


Fig. 11. Operating condition 6 ($i0.4_T50_SR3_RH90$): Good agreement with nitrogen measurement during continuous sampling, but poor voltage model matching since flooding effects are not included in the voltage model

Fig. 11 shows a good match with the GC measurement for repeated sampling. This data set corresponds to lower operating temperature and fully humidified cathode inlet conditions which exhibit both anode and cathode channel plugging, hence the discrepancy between modeled and measured voltage. The voltage matching is not very good because the effects of flooding or plugging are not represented in the voltage model. Cathode flooding and plugging are responsible for almost 20mV of voltage loss, which can be recovered by the cathode surges at $t=1000s$, and $t=3400s$. The membrane water content distribution, shown in Fig. 12 is much more uniform due to the humidified cathode inlet conditions and does not

change over the purge cycle as in the previous cases.

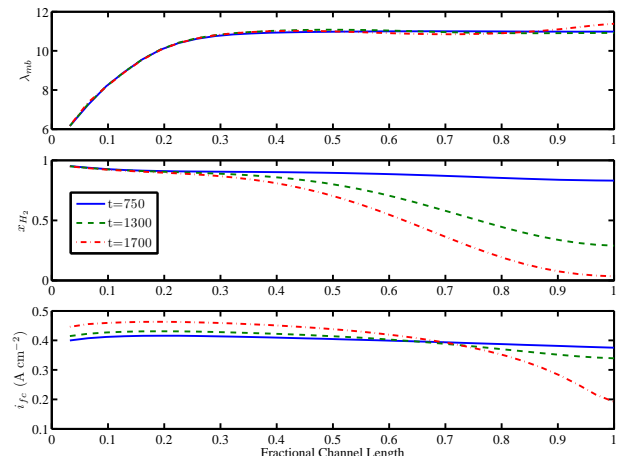


Fig. 12. The first subplot shows a snapshot of the membrane water content along the length of the channel for three times shown in Fig. 11; after a purge (before surge), mid cycle and before the next purge. The second subplot shows the hydrogen mole fraction along the length of the channel. The final subplot shows the current density distributions. Notice the different membrane profile due to higher cathode inlet RH, and less developed nitrogen front.

The parameters α_{N_2} , and D_{H_2,N_2} affect the rate of nitrogen front propagation and the delay before the voltage decay changes slope as seen in Fig. 8. Nitrogen front propagation is also weakly dependent on the current density distribution $i_{fc}(y)$, since the consumption of hydrogen drives convection in the channel. The slope of voltage drop depends on membrane/GDL resistance, the nitrogen diffusion rate and the nitrogen front propagation speed.

A. Effect of Operating Conditions

Figures 13 and 14 show the effects of increasing temperature and current density respectively. Increasing temperature increases both permeation through the membrane and to a small extent diffusion. The increased nitrogen permeation rate leads to both a quicker formation the nitrogen blanket, the time at which the voltage slope changes, and the faster propagation of the blanketing front which can be seen in the steeper second slope of the voltage plot. The effect of current density is more difficult to visualize, since the voltages are very different, therefore the deviation from nominal voltage for each given current density are plotted in the first subplot of Fig.14. The second subplot shows the hydrogen and nitrogen mole fraction at the sampling location. Since the convective term in (1) is proportional to the current density, the nitrogen is pushed toward the end of the channel more quickly with increasing current density. As a result the blanketing front forms much more quickly at

high current density, but the propagation rate of the front does not increase very much because the permeation rate is constant. This can be seen in the third subplot which shows the average mole fraction of nitrogen in the anode channel, which is nearly identical for all four cases.

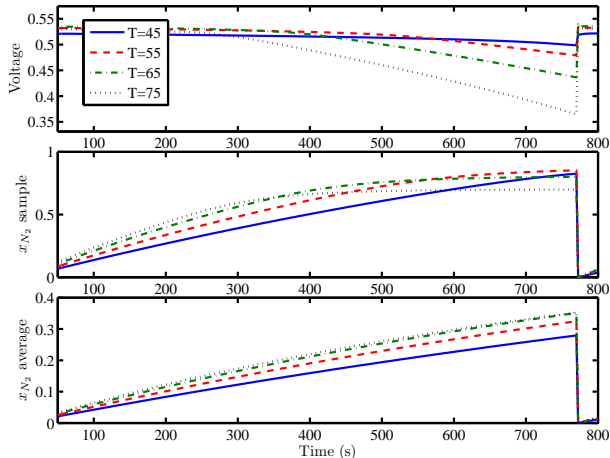


Fig. 13. Increasing temperature increases nitrogen permeation rate exponentially which leads to much faster voltage decay. The conditions for simulation are (*i*0.6_Tx_S2_RH60).

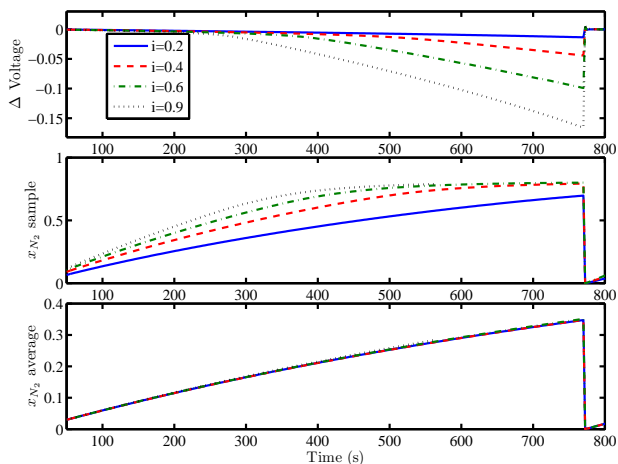


Fig. 14. Increasing current density increases nitrogen blanket formation rate, but not the accumulation rate. The conditions for simulation are (*i*x_T65_S2_RH60).

VI. CONCLUSIONS

The one dimensional anode channel model presented in this paper is able to capture and explain the observed two sloped voltage drop between purges in a PEMFC with DEA. The model shows very good results when the assumption of non-water plugging conditions are met in the channels. The evolution of a nitrogen blanketing front which leads to a hydrogen depleted region in the anode channel explains the voltage loss. Although distributed

current density measurements [40], [41] were not acquired, we can observe the effect of mass accumulation on current density distribution through the cell potential, by measuring the terminal voltage. Specifically the mass accumulation affects both the rate of voltage drop, and the time at which the steeper slope begins.

The ability of the model to predict voltage is limited, since the accumulation of liquid water in the anode channel (plugging) and cathode catalyst layer (flooding) are not included in the model, but the voltage degradation and nitrogen accumulation rates match well when the assumption of non-flooding and non-plugging conditions are valid. In the future we plan to incorporate these effects into the model. The effects of nitrogen and liquid water accumulation can be parametrized by utilizing the measurement of liquid water from neutron imaging along with the GC measurements for combinations of wet and dry channel conditions. The data set corresponding to operating condition 6, shown Fig. 11, could be used for parameterizing the liquid water effect, using the model of nitrogen accumulation which is calibrated for drier (non-flooding/plugging) conditions.

VII. APPENDIX: NOMENCLATURE AND CONSTANTS

TABLE II
TUNED PARAMETERS

$i_{o,ref,ca}$	7E-8 (A cm ⁻²)	Cathode exchange current
$i_{o,ref,an}$	0.05 (A cm ⁻²)	Anode exchange current
i_{loss}	1E-3 (A cm ⁻²)	Crossover current
D_{eff}	0.35	Effective Diffusivity in GDL
R_{GDL}	0.275 (Ω cm ²)	Contract resistance
α_{N_2}	2	N ₂ perm scale factor

VIII. APPENDIX: GC CALIBRATION

The injection port, inside the GC, was maintained at 100 °C and the column at 30 °C. A Thermal Conductivity Detector (TCD) was used for gas detection. The TCD was operated at 100 °C, and 90 mA current.

Two mass flow controllers were used to create dry gas mixtures of known (H₂/N₂) concentration in the anode channel for calibration of the GC detector. Calibration data was collected with the anode channel at 4.5 Psig operating pressure and a nominal temperature of T=60 °C. A six point calibration was used, with 5 samples repeated for each point. Fig. 15, demonstrates the linearity of the GC measurement. The detector is much more sensitive to nitrogen, due to the choice of carrier gas. The average N₂ response is 1163897 (area units / x_{N_2}), and the average hydrogen response is 24416 (area units/ x_{H_2}).

TABLE III
CONSTANTS

E_{N_2}	24000 (J mol ⁻¹)	[39]
T_{ref}	303 (K)	[39]
R	8.314	Universal gas constant
V_w	1.81×10^{-5}	Water Volume [26]
V_{mb}	5.59×10^{-4}	Membrane Volume [26]
K_{mb}	0.25	Membrane water uptake
n	2	Electron transfer #
F	96485 (C mol ⁻¹)	Faraday's Constant
C_{ref,O_2}	40.87 (mol m ⁻³)	
C_{ref,H_2}	40.87 (mol m ⁻³)	
E_c	66000 (J mol ⁻¹)	[30]
T_0	298.15 (K)	ref Temperature
$\alpha_{a,a}$	0.5	
$\alpha_{c,a}$	0.5	
D_{12}	2.56 E-6 (m ² s ⁻¹)	D_{H_2O,N_2} [25]
D_{13}	8.33 E-6 (m ² s ⁻¹)	D_{H_2,N_2} [42]
D_{23}	9.15 E-6 (m ² s ⁻¹)	D_{H_2O,H_2} [25]
$w_{an,ch}$	0.0021 (m)	An Ch width
$w_{an,rib}$	8.38E-4 (m)	An rib width
Δ_{mb}	25 (μ m)	Membrane thickness
$h_{an,ch}$	0.0018 (m)	An Ch height
L_{ch}	0.0727 (m)	Channel length
Δ_{GDL}	3.36E-4 (m)	Compressed GDL thickness
N_{sample}	9.2e-7 (mol s ⁻¹)	Sample flow rate
N_{purge}	5e-3 (mol s ⁻¹)	Purge flow rate

Since measurement of H₂O was not possible, during fuel cell operation we assume that the concentration of vapor in the anode is equal to the saturation value and hence only temperature dependent.

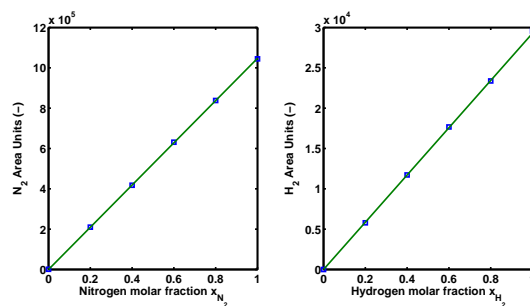


Fig. 15. GC linear response, with variation in nitrogen concentration

REFERENCES

[1] A. Karnik, J. Sun, and J. Buckland, "Control analysis of an ejector based fuel cell anode recirculation system," in *American Control Conference, 2006*, June 2006, pp. 6 pp.--.

[2] R. K. Ahluwalia and X. Wang, "Fuel cell systems for transportation: Status and trends," *J. Power Sources*, vol. 177, no. 1, pp. 167 – 176, 2008.

[3] E. A. Müller, F. Kolb, L. Guzzella, A. G. Stefanopoulou, and D. A. McKay, "Correlating nitrogen accumulation with temporal fuel cell performance," *Journal of Fuel Cell Science and Technology*, vol. 7, no. 2, p. 021013, 2010.

[4] S. S. Kocha, J. D. Yang, and J. S. Yi, "Characterization of gas crossover and its implications in PEM fuel cells," *AIChE J.*, vol. 52, no. 5, pp. 1916–1925, 2006.

[5] A. Z. Weber, "Gas-crossover and membrane-pinhole effects in polymer-electrolyte fuel cells," *J. Electrochem. Soc.*, vol. 155, no. 6, pp. B521–B531, 2008.

[6] J. B. Siegel, D. A. McKay, A. G. Stefanopoulou, D. S. Hussey, and D. L. Jacobson, "Measurement of Liquid Water Accumulation in a PEMFC with Dead-Ended Anode," *J. Electrochem. Soc.*, vol. 155, no. 11, pp. B1168–B1178, 2008.

[7] C. A. Reiser, L. Bregoli, T. W. Patterson, J. S. Yi, J. D. Yang, M. L. Perry, and T. D. Jarvi, "A Reverse-Current Decay Mechanism for Fuel Cells," *Electrochem. Solid-State Lett.*, vol. 8-6, pp. A273–A276, 2005.

[8] J. P. Meyers and R. M. Darling, "Model of carbon corrosion in pem fuel cells," *J. Electrochem. Soc.*, vol. 153, no. 8, pp. A1432–A1442, Aug. 2006.

[9] R. Borup, J. Meyers, B. Pivovar, Y. S. Kim, R. Mukundan, N. Garland, D. Myers, M. Wilson, F. Garzon, D. Wood, P. Zelenay, K. More, K. Stroh, T. Zawodzinski, J. Boncella, J. E. McGrath, M. Inaba, K. Miyatake, M. Hori, K. Ota, Z. Ogumi, S. Miyata, A. Nishikata, Z. Siroma, Y. Uchimoto, K. Yasuda, K.-i. Kimijima, and N. Iwashita, "Scientific Aspects of Polymer Electrolyte Fuel Cell Durability and Degradation," *Chemical Reviews*, vol. 107, no. 10, pp. 3904–3951, 2007.

[10] E. Kimball, T. Whitaker, Y. G. Kevrekidis, and J. B. Benziger, "Drops, slugs, and flooding in polymer electrolyte membrane fuel cells," *AIChE J.*, vol. 54, no. 5, pp. 1313–1332, 2008.

[11] C. H. Woo and J. Benziger, "PEM fuel cell current regulation by fuel feed control," *Chem. Eng. Sci.*, vol. 62, no. 4, pp. 957–968, Feb. 2007.

[12] E. Kumbur, K. Sharp, and M. Mench, "Liquid droplet behavior and instability in a polymer electrolyte fuel cell flow channel," *J. Power Sources*, vol. 161, no. 1, pp. 333–345, Oct. 2006.

[13] F. Y. Zhang, X. G. Yang, and C. Y. Wang, "Liquid Water Removal from a Polymer Electrolyte Fuel Cell," *J. Electrochem. Soc.*, vol. 153, no. 2, pp. A225–A232, 2006.

[14] J. Benziger, "Fan the flame with water: Current ignition, front propagation and multiple steady states in polymer electrolyte membrane fuel cells," *AIChE J.*, vol. 55, no. 12, pp. 3034–3040, 2009.

[15] L. Dumercy, M.-C. Pra, R. Glises, D. Hissel, S. Hamandi, F. Badin, and J.-M. Kauffmann, "PEFC Stack Operating in Anodic Dead End Mode," *Fuel Cells*, vol. 4, pp. 352 – 357, 2004.

[16] W. Baumgartner, P. Parz, S. Fraser, E. Wallnfer, and V. Hacker, "Polarization study of a PEMFC with four reference electrodes at hydrogen starvation conditions," *J. Power Sources*, vol. 182, no. 2, pp. 413–421, Aug. 2008.

[17] S. Hikita, F. Nakatani, K. Yamane, and Y. Takagi, "Power-generation characteristics of hydrogen fuel cell with dead-end system," *JSAE Review*, vol. 23, pp. 177–182, 2002.

[18] H. Li, Y. Tang, Z. Wang, Z. Shi, S. Wu, D. Song, J. Zhang, K. Fatih, J. Zhang, H. Wang, Z. Liu, R. Abouatallah, and A. Mazza, "A review of water flooding issues in the proton exchange membrane fuel cell," *J. Power Sources*, vol. 178, no. 1, pp. 103 – 117, 2008.

[19] D. Hussey, D. Jacobson, and M. Arif, "In situ fuel cell water metrology at the NIST neutron imaging facility," *Proceedings of the ASME International Conference on Fuel Cell Science, Engineering and Technology*, 2007.

- [20] D. Kramer, J. Zhang, R. Shimoï, E. Lehmann, A. Wokaun, K. Shinohara, and G. G. Scherer, "In situ diagnostic of two-phase flow phenomena in polymer electrolyte fuel cells by neutron imaging: Part A. Experimental, data treatment, and quantification," *Electrochim. Acta*, vol. 50, no. 13, pp. 2603–2614, Apr. 2005.
- [21] S. Basu, C.-Y. Wang, and K. S. Chen, "Phase change in a polymer electrolyte fuel cell," *Journal of The Electrochemical Society*, vol. 156, no. 6, pp. B748–B756, 2009.
- [22] R. Fluckiger, S. A. Freunberger, D. Kramer, A. Wokaun, G. G. Scherer, and F. N. Buchi, "Anisotropic, effective diffusivity of porous gas diffusion layer materials for PEFC," *Electrochim. Acta*, vol. 54, no. 2, pp. 551–559, Dec. 2008.
- [23] P. Chang, G.-S. Kim, K. Promislow, and B. Wetton, "Reduced dimensional computational models of polymer electrolyte membrane fuel cell stacks," *Journal of Computational Physics*, vol. 223, no. 2, pp. 797–821, May 2007.
- [24] N. R. Amundson, T.-W. Pan, and V. I. Paulsen, "Diffusing with stefan and maxwell," *AIChE J.*, vol. 49, no. 4, pp. 813–830, 2003.
- [25] T. Berning and N. Djilali, "A 3D, Multiphase, Multicomponent Model of the Cathode and Anode of a PEM Fuel Cell," *J. Electrochem. Soc.*, vol. 150, no. 12, pp. A1589–A1598, Dec. 2003.
- [26] S. Ge, X. Li, B. Yi, and I.-M. Hsing, "Absorption, Desorption, and Transport of Water in Polymer Electrolyte Membranes for Fuel Cells," *J. Electrochem. Soc.*, vol. 152, no. 6, pp. A1149–A1157, 2005.
- [27] M. Adachi, T. Navessin, Z. Xie, B. Frisken, and S. Holdcroft, "Correlation of in situ and ex situ measurements of water permeation through nafion nre211 proton exchange membranes," *J. Electrochem. Soc.*, vol. 156, no. 6, pp. B782–B790, 2009.
- [28] P. W. Majsztrik, M. B. Satterfield, A. B. Bocarsly, and J. B. Benziger, "Water sorption, desorption and transport in Nafion membranes," *J. Membr. Sci.*, vol. 301, no. 1-2, pp. 93–106, Sep. 2007.
- [29] D. A. McKay, J. B. Siegel, W. Ott, and A. G. Stefanopoulou, "Parameterization and prediction of temporal fuel cell voltage behavior during flooding and drying conditions," *J. Power Sources*, vol. 178, no. 1, pp. 207–222, Mar. 2008.
- [30] R. P. O'Hayre, S.-W. Cha, W. Colella, and F. B. Prinz, *Fuel Cell Fundamentals*. Hoboken, NJ: Wiley, 2006.
- [31] M. M. Mench, *Fuel cell engines*. Hoboken, N.J.: John Wiley & Sons, 2008.
- [32] J. S. Newman., *Electrochemical systems*, 2nd ed. Englewood Cliffs, N.J: Prentice Hall, 1991.
- [33] F. Barbir, *PEM Fuel Cells: Theory and Practice*. Burlington, Ma: Elsevier, 2005.
- [34] D. M. Bernardi and M. W. Verbrugge, "A Mathematical Model of the Solid-Polymer-Electrolyte Fuel Cell," *J. Electrochem. Soc.*, vol. 139, no. 9, pp. 2477–2491, 1992.
- [35] A. Katsaounis, S. Balomenou, D. Tsiplakides, M. Tsampas, and C. Vayenas, "The role of potential-dependent electrolyte resistance in the performance, steady-state multiplicities and oscillations of PEM fuel cells: Experimental investigation and macroscopic modelling," *Electrochim. Acta*, vol. 50, no. 25-26, pp. 5132–5143, Sep. 2005.
- [36] T. Springer, T. Zawodzinski, and S. Gottesfeld, "Polymer Electrolyte Fuel Cell Model," *J. Electrochem. Soc.*, vol. 138, no. 8, pp. 2334–2341, 1991.
- [37] J. B. Siegel, S. Yesilyurt, and A. G. Stefanopoulou, "Extracting Model parameters and Paradigms from Neutron Imaging of Dead-Ended Anode Operation," in *Proceedings of FuelCell2009 Seventh International Fuel Cell Science, Engineering and Technology Conference*, 2009.
- [38] J. Nam and M. Kaviany, "Effective diffusivity and water-saturation distribution in single and two-layer PEMFC diffusion medium," *Int. J. Heat Mass Transfer*, vol. 46, pp. 4595–4611, 2003.
- [39] R. Ahluwalia and X. Wang, "Buildup of nitrogen in direct hydrogen polymer-electrolyte fuel cell stacks," *J. Power Sources*, vol. 171, no. 1, pp. 63–71, Sep. 2007.
- [40] H. Ju and C. Wang, "Experimental Validation of a PEM Fuel Cell Model by Current Distribution Data," *J. Electrochem. Soc.*, vol. 151, no. 11, pp. A1954–A1960, 2004.
- [41] S. A. Freunberger, M. Reum, J. Evertz, A. Wokaun, and F. N. Buchi, "Measuring the Current Distribution in PEFCs with Sub-Millimeter Resolution," *J. Electrochem. Soc.*, vol. 153, no. 11, pp. A2158–A2165, 2006.
- [42] R. Taylor and R. Krishna, *Multicomponent mass transfer*. New York: Wiley, 1993.